Comparison of Inlet Broadband Acoustic Liner Predictions to Quiet Technology Demonstrator 3 Flight Data

Jason C. June*, Eric Nesbitt [†], Douglas M. Nark [‡], and Michael G. Jones[§]

NASA Langley Research Center, Hampton, VA 23681, USA

Companion acoustic liner attenuation predictions and flight data representative of certification conditions are analyzed to determine the validation quality and gain an understanding of current prediction shortcomings. These comparisons are limited to the inlet broadband component of fan noise. Two prediction methods are assessed: a traditional, semiempirical model, and a computational approach with a parabolic duct propagation code coupled with a Ffowcs Williams-Hawkings solver for free-field propagation. The semiempirical method is widely used for aircraft system noise predictions, but does not explicitly account for several physical parameters important for sound attenuation. The computational approach includes these effects, but requires a significant increase in cycle time. For the three-degree-of-freedom (3DOF) liner tested, both methods have a bias error less than 0.5 dB for cutback and takeoff power settings, and a much larger 3–4 dB bias for approach power setting. The standard deviation of each method varies between 1–2 dB for different conditions. The similar performance of both approaches illustrates that, in this instance, the additional complexity of the computational approach does not provide a clear improvement over the semiempirical method. Planned improvements to the numerical grid and source assumptions may result in reevaluation of this conclusion in later work.

Nomenclature

a	=	polynomial coefficients
$\mathcal{A}$	=	attenuation
B	=	bandwidth
$\mathcal{B}$	=	one-third octave band number
c	=	sound speed
D	=	average duct diameter
$\delta\mathcal{A}$	=	maximum absolute deviation of sample and population mean attenuation estimate
$\delta\sigma_{\mathcal{A}}$	=	maximum absolute deviation of sample and population attenuation standard deviation estimate
δf	=	power spectrum conversion binwidth
Δf	=	integration frequency binwidth
L	=	liner length
N	=	number of samples
P, p	=	one-third octave band, narrowband root-mean-squared acoustic pressures
S	=	simulation budget (total sample count)
W	=	acoustic power
w	=	weight
x, y, z	=	Cartesian coordinates
η	=	frequency parameter, fD/c
θ	=	polar (emission) angle
σ	=	standard deviation
φ	=	azimuthal angle

---

*Research Aerospace Engineer, Aeroacoustics Branch, MS 461, AIAA Senior Member
[†] Senior Research Engineer, Aeroacoustics Branch, MS 461, AIAA Senior Member
[‡] Senior Research Scientist, Structural Acoustics Branch, MS 463, AIAA Associate Fellow
[§] Senior Research Scientist, Structural Acoustics Branch, MS 463, AIAA Associate Fellow

Subscripts
f =   frequency
H =   hilite
h =   hardwall
i, j =   indices
l =   lined
r =   realization
S =   source
Superscripts
‾   =   ensemble average
ˆ   =   population parameter estimate

I. Introduction

R<small>EDUCING</small> noise emissions of future commercial aircraft for near-airport communities remains a challenge. NASA is committed to ameliorating the impacts of noise emissions, working toward goals established in the Aeronautics Strategic Implementation Plan [1]. Fan noise (including propulsion-airframe aeroacoustic and acoustic liner effects) will play a significant role in shaping the overall noise signature of future commercial aircraft. Accurate, physics-based prediction of each of these effects is critical to the quality of system noise assessments of aircraft concepts and noise reduction technologies.

As a step toward this goal, two acoustic liner prediction tools in use at NASA are assessed relative to flight test data from the Quiet Technology Demonstrator 3 (QTD3) campaign [2–4]. QTD3 was a focused effort using a 737 MAX-7 to determine the in-flight performance of a three-degree-of-freedom (3DOF) liner, designed using the process in Nark and Jones [4]. Additional analysis of QTD3 test data is undertaken to better understand and predict the acoustic liner attenuation of the inlet fan noise component. The existing comparison of far-field QTD3 attenuation data with a Boeing tool [2], Grazing flow Ray acoustics (GRays), is complemented by a comparison with two additional prediction tools: a semiempirical correlation developed by Kontos et al. [5] and a computational approach using the duct propagation and free-field radiation capabilities of CDUCT-LaRC (CDL) [6]. This comparison is made on a lossless hemisphere basis. Inputs to the computational prediction are altered to predict the "as-built" liner impedance rather than the "as-designed" impedance used in a previous study [4]. Lastly, the azimuthal asymmetry noted by Nark and Jones [4] in the attenuation predictions is explored.

The primary purpose of this paper is to benchmark and analyze the performance of CDL relative to flight test data. This analysis is limited to the broadband acoustic liner attenuation of the fan inlet noise for both prediction and flight data. The tones have been separated from the flight data, and there is no attempt to predict tone attenuation. A second purpose is to evaluate CDL as a potential replacement for the method of Kontos et al. [5] in the Aircraft NOise Prediction Program (ANOPP) [7] for system noise acoustic liner applications. While CDL could be used directly for individual assessments, a surrogate model would be more compatible with system noise requirements as well as optimization studies.

The paper is organized by first presenting the details of the tools and flight test setup used to generate the data in Section II. Then details of the CDL sampling parameters and post-processing to one-third octave band data are discussed in Section III, followed by the results in Section IV, and ending with plans for future work in Section V.

II. Tools and Setup

Background is provided for both the experimental data set and the liner prediction methods for context of the comparison. The validation here is an independent supplement to the comparisons in Wong et al. [2] that used GRays for far-field liner attenuation predictions.

A. Flight Test Setup

As discussed previously, QTD3 served as a testbed to assess the merits of the liner design strategy of Nark and Jones [4]. Extensive test details may be found in Wong et al. [2] and Brusniak et al. [3]; only a summary is reproduced here. The test included two configurations: one with the 3DOF inlet barrel liner installed, and one where it was taped over to simulate a hardwalled duct. The forward fan case was also hardwalled to isolate the performance of the barrel liner. The

noise levels were recorded using an ensemble linear array and a phased array underneath the flight track. The data were then processed and normalized with the method outlined in Wong et al. [2], using information from both arrays to produce the one-third octave band data used in these comparisons. The liner attenuation was experimentally measured to be the difference of the two configurations. One-third octave band data are generally available for bands 24–37, where the band number $\mathcal{B}$ is related to the midband frequency $10^{\mathcal{B}/10}$ in Hz. At certain combinations of emission angle and engine setting, the signal-to-noise ratio is too low to reliably use for comparison with the prediction models for a subset of those bands. The data from three engine power settings will be used for comparison, representative of approach, cutback, and full-power takeoff conditions.

B. Computational Attenuation Prediction

Similarly, the computational liner prediction method used here is thoroughly described in Nark and Jones [4]. The salient details of the process are summarized, along with some additional information on the source assumptions. The only difference of note in the present calculations is that the specified liner impedance values have been modified since Nark and Jones [4]. That paper used the as-designed facesheet thicknesses of 0.032 in, but the as-built (tested) value of 0.055 in thickness is used here. The other modification is a change to the impedance model used to account for the resistance values of non-circular orifice geometry on the liner facesheet. Details of this model change will be addressed in a future publication.

In the first stage of computation, an acoustic potential distribution is defined at the fan face and propagated forward to the inlet hilite using CDUCT-LaRC (CDL). CDL is a duct propagation code utilizing a parabolic approximation [8, 9] to the convected Helmholtz equation. Here, as in the general case where a priori source information is limited, the acoustic potential distribution is specified as a coherent combination of circular duct modes with modal coefficients of random phase and amplitude [10, 11]. The phase angle of the modal coefficient is drawn from a continuous uniform random distribution over 0–360 deg, while the amplitude comes from a standard (i.e., between 0 and 1) uniform random distribution.* The fan face acoustic potential distribution is marched forward in a nominally axial direction in curvilinear coordinates to the nacelle hilite. The underlying mean flow solution is estimated from a one-dimensional isentropic flow using a known Mach number at the fan face. The process of drawing random amplitudes and phases for the included modes is repeated, to build many realizations of the fan face acoustic potential distribution. The collection of these realizations is a statistical representation of the source. For each realization of fan face acoustic potential distribution, a pair of propagation simulations are carried out, one in a hardwalled duct and one with a lined surface. The estimates of liner attenuation are calculated from the difference of these paired simulations.

Choice of source modal content has significant impact on the accuracy of the results of duct propagation and subsequent radiation, and deserves additional attention. The typical choice for broadband noise is to equally weight all modes (with a cutoff ratio greater than unity) in the absence of additional information. Predictions are typically improved if experimentally-obtained modal distributions are used [12, 13]. For the general, predictive capability sought here, the statistical equivalent to equally weighted modes is used, with some minor modifications.

The first is a restriction on the cutoff ratio to a value greater than 1.25 in an effort to eliminate the modal content that would propagate at high angles to the duct axis, inconsistent with the parabolic approximation. Figure 1 shows the radial and positive circumferential modes with the requisite cutoff ratio to be included in the source specification for the highest simulated frequency, 5623 Hz. Note that the corresponding negative circumferential modes within the bounds are also included in the simulation even though they are not plotted. Also shown are the additional restrictions that are placed on the modal content in the maximum allowable radial and circumferential mode. These prescribed limits are an effort to keep the input modal content resolvable on the computational grid, not a limitation of CDL itself. The grid has 181 circumferential nodes and 65 in the transverse direction. In the circumferential direction, the maximum mode limit of 75 is chosen to keep slightly more than two points per mode order. In the transverse direction a more conservative rule of thumb is used, keeping at least six nodes per mode order and limiting the radial order to 10. The range of simulated frequencies covers one-third octave bands 24–37 (355–5623 Hz). Using a single grid to cover this wide frequency range led to compromises in the grid density; CDL requires that the transverse node spacing relative to the wavelength not be too large (see Dougherty [14] for additional discussion). In subsequent work, this will be resolved by using a multigrid approach described in Nark et al. [15].

Ultimately, the goal is to simulate a sufficiently random source, and the prescribed modal content for CDL still allows for a large number of modes to be included. Rice [16] developed a correlation for attenuation that uniquely depends on cutoff ratio, with the assumption that power is not concentrated in a few low order radial modes. The cutoff

---

*CDL is a linear code; results are unaffected by scaling to match the input sound pressure level.
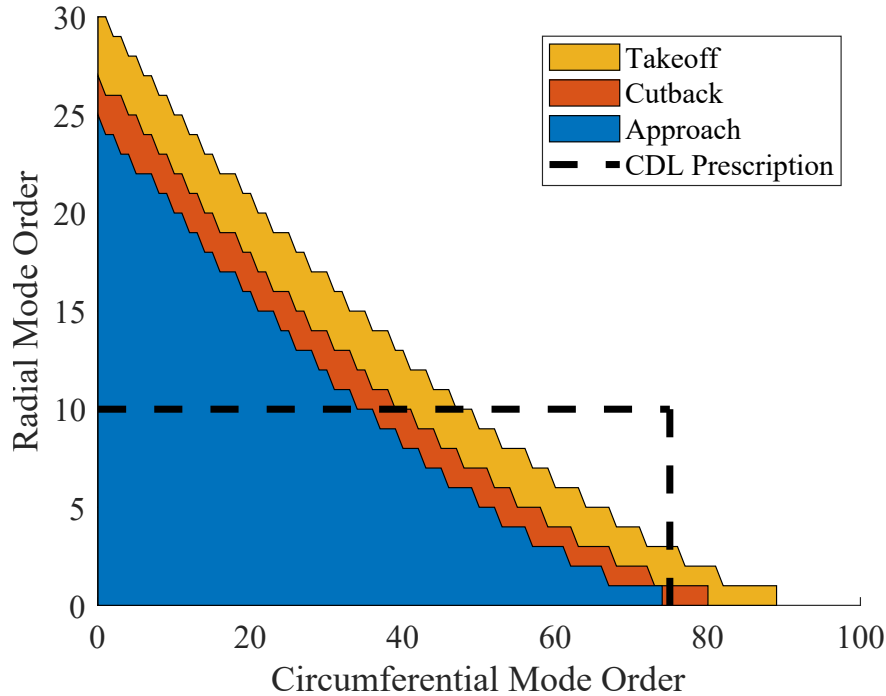
Fig. 1 The positive circumferential modes with a cutoff ratio greater than 1.25 are shown as a shaded region for all three certification conditions at the band 37 upper band edge 5623 Hz. Also shown are the prescribed limits on the CDL modal content.

ratio is also related to the peak radiation angle [17]. With this in mind, it is expected that so long as there are a sufficient number of modes propagating in the duct, the distribution of the cutoff ratios associated with these modes does not have any large gaps in values. Adding additional modes with similar cutoff ratios does not meaningfully impact the far-field attenuation because the peak angle for the additional mode closely matches that of a mode already included in the simulation, and both have similar attenuations. While this assumption will fail at low frequencies when few modes are propagating, it should have minimal practical impact on the present results. All modes with cutoff ratios greater than 1.25 are within the prescribed limitations on the CDL source specification below 1900 Hz, (i.e., the limits have no impact below this frequency).

A two-dimensional slice of the computational grid along the centerline of the duct is shown in Fig. 2a. As will be discussed in Section IV.A, there were two different grids generated: an initial grid that was used in Nark and Jones [4], and the current grid used for the results presented here. The difference in the grids primarily concerns definition of the surface at the upstream domain boundary, as well as the region of large area increase near the nacelle lip. Figure 2b defines the far-field propagation angles relative to the nacelle geometry.

Another important point is the assumed modal content. It is based on cutoff criteria for a hardwalled, axisymmetric circular duct with uniform flow, whereas the actual geometry is not axisymmetric. The simulated fan source plane is annular due to the presence of the spinner, and upstream of the spinner a thin, artificial centerbody is retained as CDL is limited to annular duct geometries. The upper surface of the centerbody corresponds to the linear portion of the lower boundary in Fig. 2a (not pictured in Fig. 2b). This artificial centerbody has a diameter nominally 8.5 % of the fan face diameter. Additional simulations were run using annular duct modes. For low frequencies, these were in agreement with the circular duct mode results. However, at higher frequencies the annular duct modes produced nonphysical results. This typically occurs when the artificial centerbody diameter is too small. Instead of increasing the centerbody diameter to use annular duct modes, the less sensitive circular modes were retained for use.

Following propagation to the hilite, the solution is used to generate a permeable data surface that is used as input to the Ffowcs Williams-Hawkings (FW-H) equation and radiated to the desired far-field observers covering a portion of a 150 ft radius sphere. Conversion between frequency and time domain calculations follows the standard time-harmonic relationship. A two-degree emission angle (θ) resolution is used for the prediction over 30–90 deg to match the experimental data resolution. Visual comparison is carried out at a ten-degree resolution, also matching the resolution
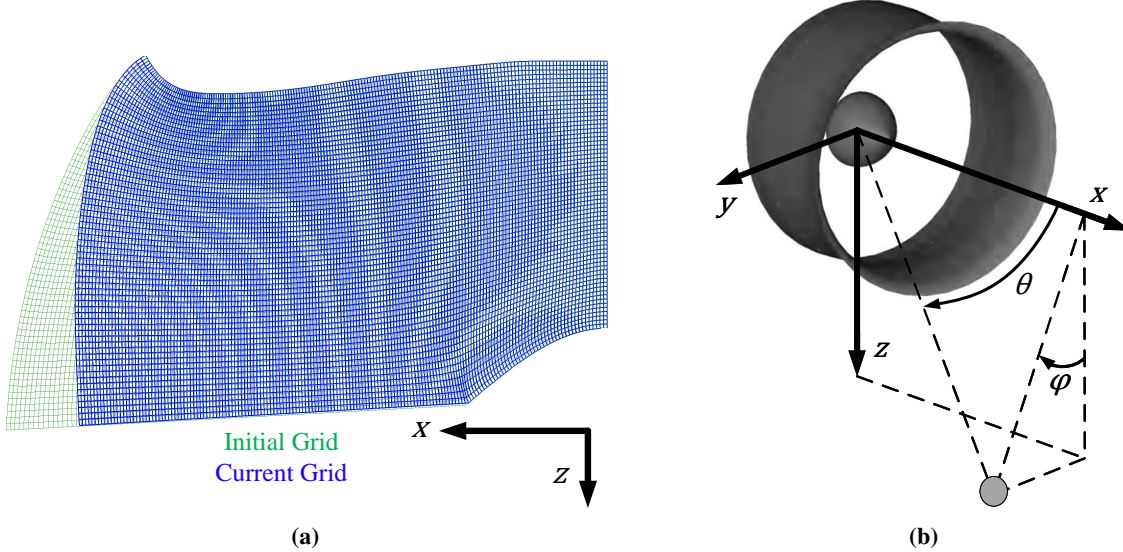
Fig. 2 The initial and current grids for the upper half of the centerline plane are displayed in (a). The coordinate system and far-field angle definition for the far-field propagation are shown in (b).

reported in [2]. While comparisons with flight test data only require observers on the hemispherical arc under the flight track, additional observers are placed at sideline angles in the forward hemisphere. These sideline observers have the same emission angle distribution as the observers in the flight track plane and an azimuthal resolution of two degrees over the range of 0–60 deg elevation angle. These observers are used to more completely address the prediction asymmetry noted in Nark and Jones [4] and clarify that while the results are not axisymmetric, the port-starboard geometric symmetry is preserved under the assumed source conditions, as all modes in the source description are equally weighted. The previous statement applies to statistical quantities; individual realizations of the fan face acoustic potential distribution will be asymmetric.

C. Semiempirical Attenuation Prediction

As mentioned previously, the model of Kontos et al. [5] is also evaluated relative to the flight test data. This model for liner attenuation is a least-squares polynomial fit of General Electric (GE) engine data as a function of polar emission angle, frequency parameter, and the ratio of liner length to duct diameter,

$$\mathcal{A} = \frac{\eta L}{D} \sum_{i=0}^{4} \sum_{j=0}^{6} a_{ij} \theta^j \left(\log \eta\right)^i . \tag{1}$$

The coefficients a_{ij} were determined in a sequential procedure rather than a single least-squares evaluation. First, fourth-order polynomials were fit to $\mathcal{A}$ as a function of $\log(\eta)$ for each individual polar angle where data were available. In a second step, each set of coefficients of a given order were fit as a sixth-order function of polar angle. Notably, there is no azimuthal angle or flight Mach number dependence.

A common concern with empirical modeling approaches is the possibility of overfitting. Kontos et al. [5] notes that this restriction limits applicability of this method to those liner designs entering service contemporaneously with the data in the prediction method. The engines used had double-degree-of-freedom liners, and the accuracy of this method to predict an 3DOF liner is potentially limited.

III. Computational Simulation Sampling Parameters and Processing

The CDL discrete frequency far-field results must be post-processed to one-third octave band values for comparision with flight data. As a first step, it is assumed that the power spectrum is constant over an arbitrarily small bin width, δf, so that the power spectrum can be converted to an equivalent narrowband power spectral density function. Having

5

converted to power spectral density, the next step is to choose an integration method and the associated sampling parameters.

A general integration quadrature for the integrated band pressure-squared value is

$$P^2 = \Delta f \sum_{i=1}^{N_f} w_i \frac{p_i^2}{\delta f}, \tag{2}$$

where the pressure-squared value, p_i^2, at the i-th frequency is multiplied by a weight w_i and summed over the specified number of frequencies, N_f, distributed in integration band. Increasing the number of frequencies decreases the binwidth, Δf, which is related to the total bandwidth $B = (N_f - 1)\Delta f$, for uniformly spaced frequencies.

A. One-Third Octave Band Uncertainty

One consideration in choosing integration sampling parameters is the relationship with the integral uncertainty. When computational costs are relatively uniform within a band, the simulation budget may be defined as $S = N_f \cdot N_r$, where N_r is the number of realizations (assumed equal) at each frequency. For a homoskedastic narrowband spectrum with standard deviation σ, the random uncertainty for the mean integral value is proportional to $B\sigma/\sqrt{S}$, while the usual $\sigma/\sqrt{N_r}$ applies for the mean estimates of the individual narrowband frequencies. Although the random error of the mean integral value (for a fixed simulation budget) is independent of the choice of N_r and N_f, the bias error is solely a function of the binwidth. This implies a minimization of the total uncertainty as $N_r \rightarrow 1$ and $N_f \rightarrow S$.

In practice, N_r does not need to be driven to such an extreme since the bias error becomes negligible even for modest simulation budgets.[†] This is particularly true for the broadband liner attenuation, which generally has a smooth, slowly varying spectral dependence. Another common rationale for moderating extreme values of N_f and N_r is that analysis is performed on the narrowband spectra rather than the integrated band alone, thereby requiring N_r to be large enough to reduce the narrowband random uncertainty.

For the integration performed here, a constant binwidth of 1 Hz was chosen to provide a fine enough resolution to limit the bias error. This assumption has been verified via comparison and agreement of the integration results from both composite trapezoidal and Simpson's rule. A convergence study was completed to guide selection of the number of realizations at each frequency.

B. Integral Convergence

In the previous work [4], a sample size of eleven realizations of the modal amplitude and phase distributions was used at each one-third octave band center frequency. This resulted in overlapping confidence intervals in the radiated hardwall and lined sound pressure levels. This overlap primarily manifested at low polar angles, but also impacted higher polar angles where the mean trend between the hardwall and lined simulations potentially indicated a more significant attenuation. A convergence study is performed to determine the number of realizations that will resolve this issue and allow for a more confident assessment of the CDL-predicted acoustic liner far-field attenuation.

Due to computational and practical limitations, data convergence was only confirmed at a single band instead of all three flight conditions and across the full set of one-third octave bands. The intermediate power setting, cutback, was chosen to minimize any effects of the convergence on flight condition. Also note that this was the most heavily weighted power setting in the liner design process. With respect to frequency, if the same number of realizations is used at every frequency, Section III.A indicates that the uncertainty in the mean attenuation should be relatively lower with increasing one-third octave bands (increasing $N_r \cdot N_f$). The choice was made to select a central band, $\mathcal{B} = 31$, at the risk of unconverged lower frequency bands. However, the approximate effect of varying N_f is known and can be compensated for when analyzing the results. Another important distinction should be made for the results in this section. To this point, the integrated pressure spectrum of Equation 2 has been used in discussion. Ultimately, the convergence sought is the value of the liner attenuation,

$$\mathcal{A}(\theta, \varphi, \mathcal{B}) = 10 \log\left(\frac{P_h^2}{P_l^2}\right). \tag{3}$$

[†]Even for a composite trapezoidal rule scheme, a doubling of N_f will reduce the bias error by a factor of four, while the random error is reduced by a factor of $\sqrt{2}$.

Convergence trends of the average liner attenuation as a function of sample size were captured for all spatial points (see Section II.B) in the forward hemisphere at a given frequency band. The average attenuation is

$$\overline{\mathcal{A}}(\theta, \varphi, \mathcal{B}, N) = \frac{1}{N} \sum_{i=1}^{N} \mathcal{A}_i(\theta, \varphi, \mathcal{B}), \tag{4}$$

where N is the number of realizations and i is any one particular realization of attenuation. Convergence of this sample statistic is ideally measured as the number of samples required to limit the deviation to the true population statistics below a threshold condition (e.g., less than 0.05 dB). However, the population statistics are unknown and must be estimated using the sample statistics calculated with all available samples, N_r, denoted by $\hat{\mathcal{A}}$. For sample sizes $N \ll N_r$, $\hat{\mathcal{A}}$ is a reasonable approximation of the true population mean, $\overline{\mathcal{A}}(N \to \infty)$, when tabulating the deviation of sample and population statistics. However, this assumption breaks down when $N \sim N_r$, and if the acceptable deviation is not seen prior to that point, N_r must be increased to evaluate the convergence trend at higher values of N.

As mentioned previously, convergence is desired over the entire angular domain of the far-field attenuation. As such, the maximum absolute deviation over all polar and azimuthal angles is used for convergence, this maximum absolute deviation for the mean and standard deviation are defined as

$$\delta\mathcal{A}(\mathcal{B}, N) = \max_{\theta, \varphi} \left| \overline{\mathcal{A}}(\theta, \varphi, \mathcal{B}, N) - \hat{\mathcal{A}}(\theta, \varphi, \mathcal{B}) \right| \tag{5a}$$

and

$$\delta\sigma_{\mathcal{A}}(\mathcal{B}, N) = \max_{\theta, \varphi} \left| \sigma_{\overline{\mathcal{A}}}(\theta, \varphi, \mathcal{B}, N) - \sigma_{\hat{\mathcal{A}}}(\theta, \varphi, \mathcal{B}) \right|. \tag{5b}$$

The values of $\delta\mathcal{A}$ and $\delta\sigma_{\mathcal{A}}$ for the 1250 Hz one-third octave band are shown in Fig. 3 as a function of the sample size. Best fits to an $N^{-\frac{1}{2}}$ form accompany the data. These curve fits provide a useful tool for approximating an upper limit to the number of samples where the convergence trends are credible. User-defined limits on the allowable deviation are ultimately subjective. For this work, we define convergence as the number of samples required to limit the maximum deviation of the mean and standard deviation to less than 0.1 dB; conservatively, this occurs by 100 samples.

C. Integration Procedure

It is worth briefly addressing the procedure order selected to process the simulation results into attenuation values. The three steps are: taking the difference of the lined and hardwall narrowband result pairs, integration to one-third octave band, and averaging over all the realizations of modal content. In order to take advantage of the variance reduction offered by the paired simulations with the same modal content, differencing should always precede averaging. Initially, the procedure was to difference, average, then integrate. However, this order requires uncertainty propagation to estimate the uncertainty in the one-third octave band integral. Instead of using sensitivity based uncertainty propagation with assumptions on the input pressure-squared distributions, the issue can be avoided by directly computing the statistics of the integral with the sequence of integration, differencing, then averaging.

As mentioned in the previous section, integration was performed on the pressure-squared values. In the rare occasion (on the order of 0.1 %) that a CDL run fails to complete, a value must be assumed so that the one-third octave band integral can be calculated for that particular realization. The median pressure-squared value over all realizations of that frequency is substituted for these cases. The median value is used in lieu of the mean value since the pressure-squared distributions are skewed.

IV. Results

Following determination of the simulation sampling parameters, CDL is run to obtain estimates of the far-field attenuation at all relevant frequencies and flight conditions. First, some results of the in-duct attenuation are shared prior to the far-field attenuation results. Lastly, some results show the variation of the attenuation as a function of azimuthal angle.
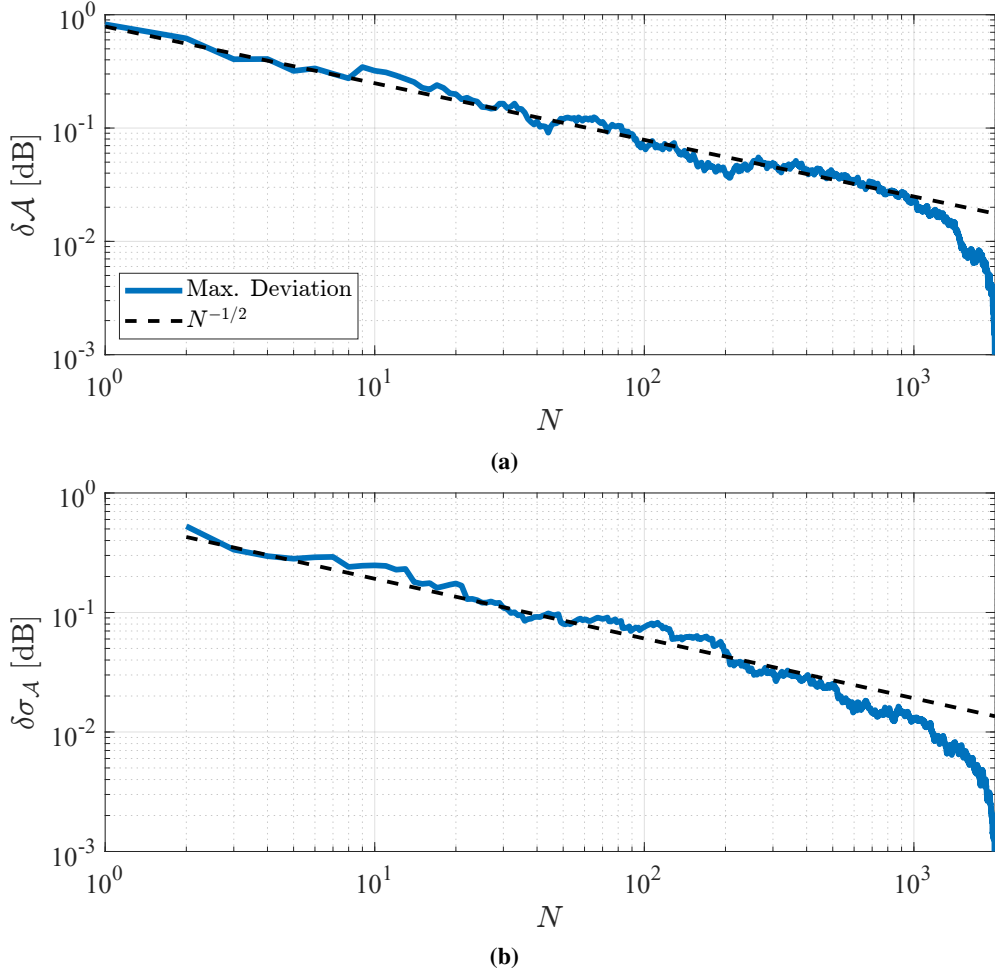
Fig. 3 **The maximum deviation over all spatial locations of the sample to estimated population mean is shown in (a), along with the theoretical $N^{-1/2}$ trend. In (b), the maximum deviation of the standard deviation is displayed. Both plots are for the one-third octave band with center frequency 1250 Hz cutback condition as a function of the number of realizations included in the sample.**

A. In-Duct Attenuation

The main result of the in-duct propagation is a measure of the attenuation by the liner in the duct. The in-duct attenuation was the metric used in Nark and Jones [4] to optimize the liner design. Typically this is measured as the difference in the power integrated across the duct cross section of the fan face relative to the duct exit. The power calculation used here is that of Eversman [18]. Figure 4 shows several examples of the change in acoustic power in the duct, W, relative to the acoustic power at the source, W_S.

Specifically, Fig. 4a shows the results of the power reduction for the takeoff condition as a function of frequency on an initial (identical to Nark and Jones [4]) and current grid. For each grid, the in-duct attenuation is shown for the hardwall and lined cases. An immediate observation is that the hardwall cases do not have the expected value of zero in-duct attenuation. Second, the results are strongly dependent on the grid generation with the current grid leading to a significant improvement over the initial grid. Inspection of a plot for a single frequency as a function of the axial grid coordinate lends some guidance as to the cause of the artificial attenuation. An example is shown in Fig. 4b for the takeoff and approach cases at 1000 Hz. The focus is on the portion of the duct upstream of the liner (only hardwall cases are plotted), as this is where the area increases most rapidly. As discussed in Dougherty [14], the parabolic approximation is derived by assuming the coupling terms with the reflected waves are negligible. Specifically, those assumptions lead to the restriction of a slowly varying Mach number and duct area, as well. This localization of the attenuation effect also explains why this behavior was not evident in Nark and Jones [4]. For the liner design, the
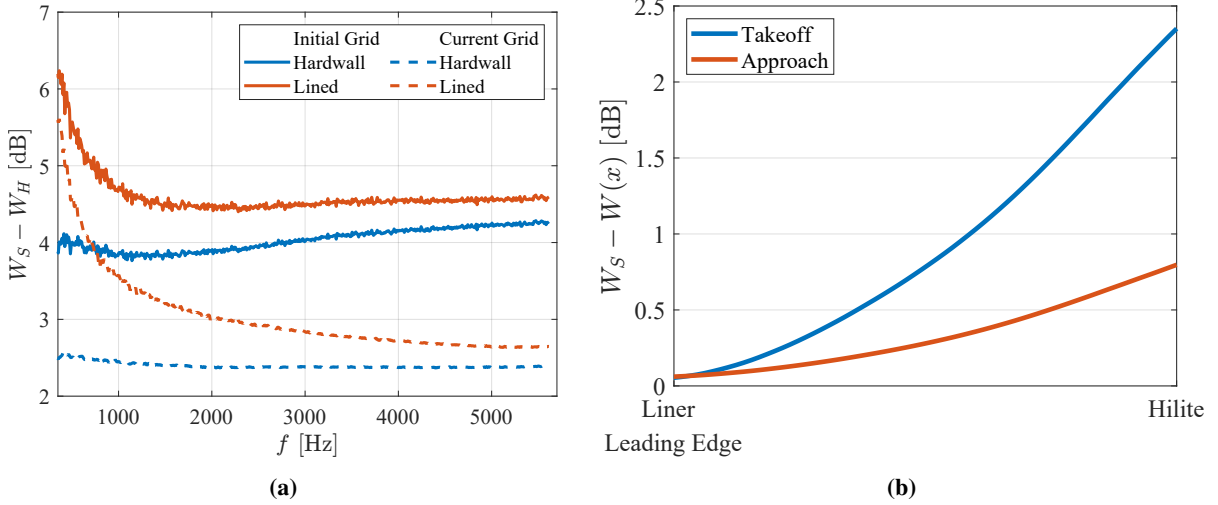
Fig. 4 **Acoustic power reduction between the source and hilite at takeoff is shown in (a) for the hardwall and lined cases on the initial and current numerical grids. The axial variation of the acoustic power in the duct at 1000 Hz is displayed in (b) for the hardwalled duct with takeoff and approach Mach numbers.**

in-duct attenuation was calculated at a location upstream of the barrel liner, but well downstream of the affected region near the hilite.

Returning to the in-duct attenuation plot (Fig. 4a), it should also be noted that the results for bands 24 and 25 are not displayed because of the a significant jump in attenuation calculated at those frequencies. This is believed to be related to the same grid spacing to wavelength restriction mentioned earlier and will likely be resolved with the use of multiple grids. For the current work, the data for those bands is not plotted for comparison with the flight test data.

The key takeaway is that the in-duct attenuation can be a useful verification of the grid quality. Additionally, it appears that there is a dependence on the mean flow solution. The hardwall attenuation measured at the hilite is nominally 1.4 and 0.7 dB for the cutback and approach conditions, respectively. Understanding the apparent Mach number dependence and continuing to reduce the attenuation seen in the hardwall cases are subjects of future work.

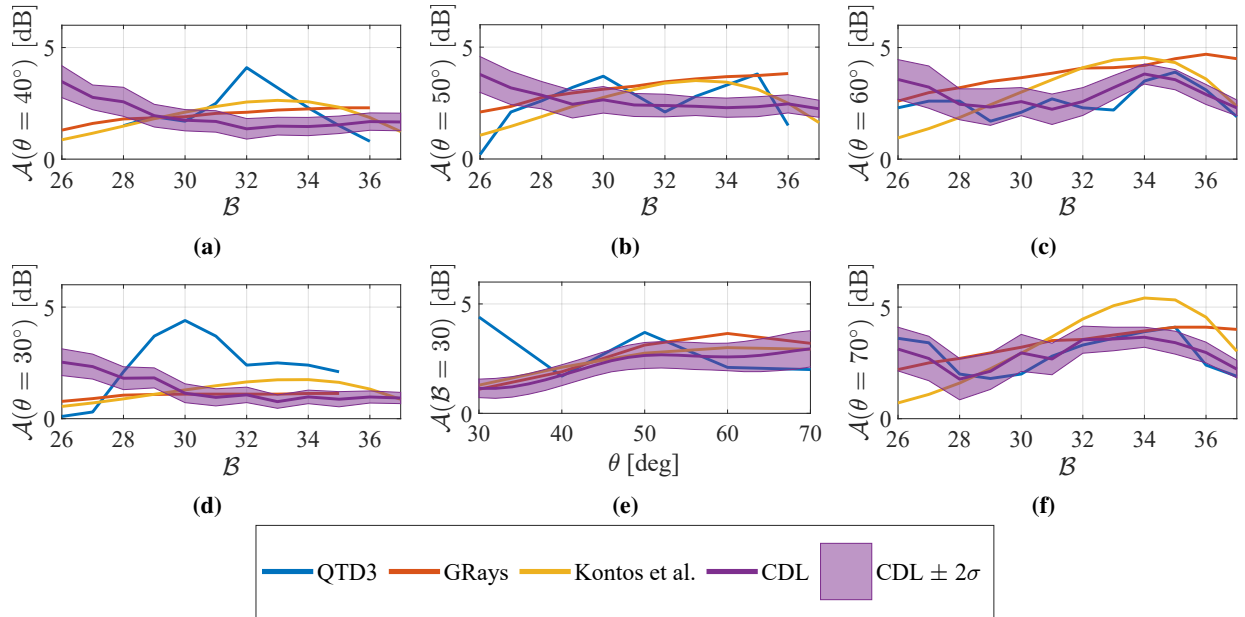### B. Far-Field Attenuation Spectra

Turning to the far-field results, a comparison is shown between the results presented in Wong et al. [2]: the QTD3 flight data and an attenuation prediction with GRays, along with the semiempirical prediction method from Kontos et al. [5] and the CDL results. In addition to the mean prediction results, an interval of two standard deviations is shown around the CDL results. This should not be interpreted as a prediction interval, as the width of the interval here is dependent on the number of frequencies included in the integration. The approach flight condition is shown in Fig. 5, cutback in Fig. 6, and takeoff in Fig. 7.

For each condition, the attenuation is shown as a function of one-third octave band number for several emission angles, increasing in value moving clockwise around the edge from the lower left. In the lower middle plots, the attenuation is replotted for band 30 to illustrate the trends as a function of emission angle. Note that the top row of plots covers the emission angles (40–60 deg) that are expected to impact the contribution of the inlet attenuation to the overall system noise. This aligns well with the expected range of angles that are well-resolved for the CDL predictions. Based on the cutoff ratio limit, a rough estimate from Rice [17] indicates that the peak radiation angle for a cutoff ratio of 1.25 is 53°. The width of the lobe is inversely proportional to frequency; nominally the upper emission angle where the results are expected to be valid increases at low frequencies.

On the whole, the three prediction methods have similar performance; the cutback and takeoff conditions have much better agreement than those for approach. CDL deviates from the flight data more than the other approach predictions at high frequencies and angles, possibly related to the assumptions and approximations used here. More generally, it does not appear that the equal energy assumption is particularly appropriate for the approach case. Data from other inlet experiments has shown that at low power settings, where the fan speed is subsonic, the broadband modal content is biased toward the corotating modes [12, 13]. A second source assumption was tested where the modal content has
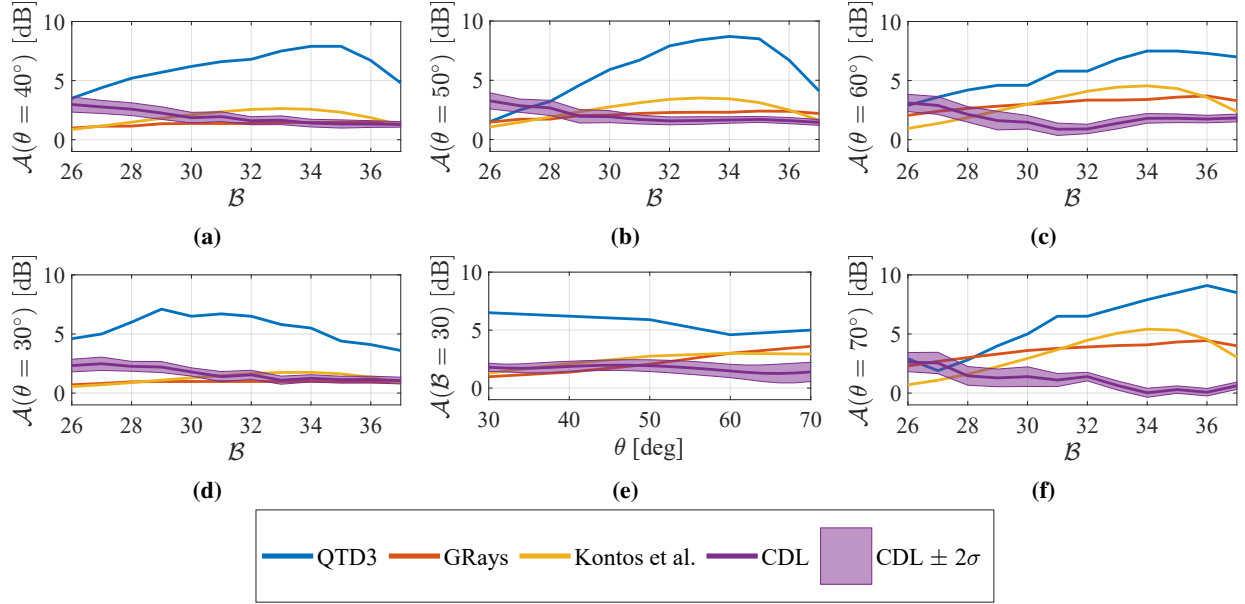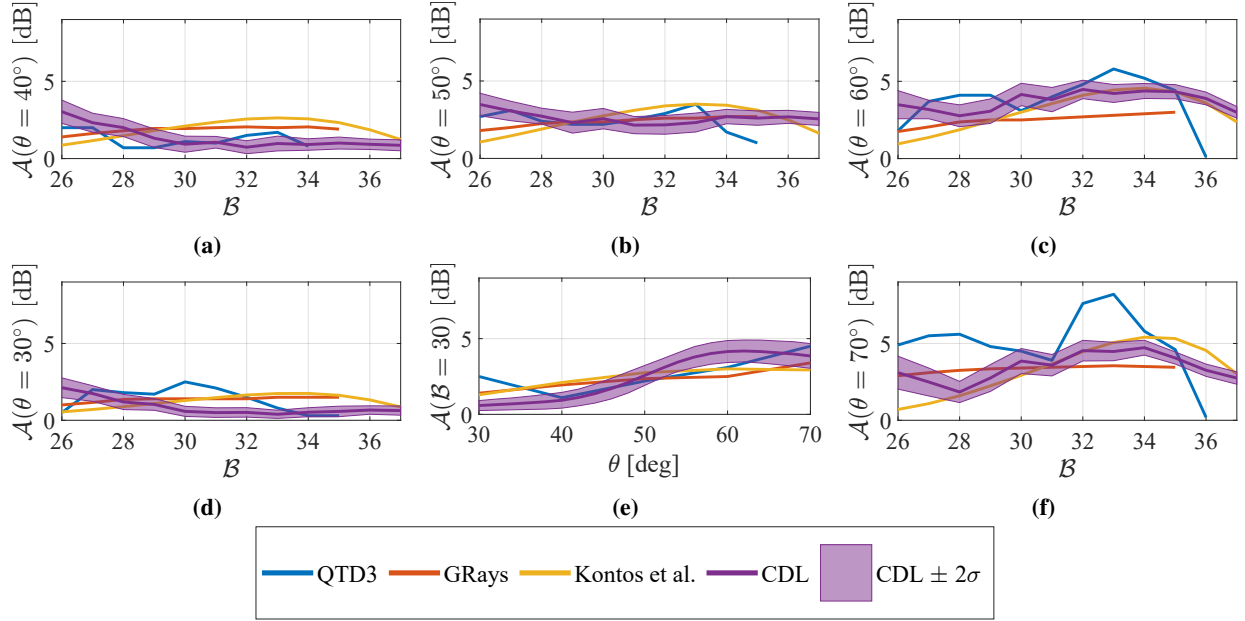
Fig. 5   Attenuation spectra are shown for all bands at several polar angles, as well as the 1000 Hz band across all polar angles. The approach condition is displayed, comparing flight data with three prediction methods.

Fig. 6   Attenuation spectra are shown for all bands at several polar angles, as well as the 1000 Hz band across all polar angles. The cutback condition is displayed, comparing flight data with three prediction methods.

the same specificiation as that described in Section II.B with the one exception – that all counterrotating modes were excluded. However, this did not yield a significant improvement and is not shown here.

The bias error and variance of each prediction method are calculated relative to the flight test data. Inspection of trends as functions of frequency and angle do not yield any particularly helpful differentiation between where a particular method consistently outperforms another. Table 1 shows the bias and standard deviation for each of the methods broken out by flight condition; all angles and bands are used in the calculation. These values quantitatively support the preceding conversation on the relative strengths of each method.

10

Fig. 7 Attenuation spectra are shown for all bands at several polar angles, as well as the 1000 Hz band across all polar angles. The takeoff condition is displayed, comparing flight data with three prediction methods.

Table 1 The bias error and standard deviation over all angles and bands are tabulated for each combination of prediction method and flight condition in dB. A positive value of bias error represents underprediction of flight test measured attenuation.

Condition	Bias			Standard Deviation		
	GRays	Kontos et al.	CDL	GRays	Kontos et al.	CDL
Approach	3.1	3.1	4.1	2.1	1.4	2.4
Cutback	−0.5	−0.3	−0.1	1.3	1.4	1.3
Takeoff	0.5	0.3	0.3	1.4	2.0	1.6

C. Azimuthal Variation

In Nark and Jones [4], there was some question of whether the asymmetry in the mean far-field predictions was due to an intrinsic asymmetry, or just normal statistical variations. After looking at comparisons of both the narrowband and integrated values, it was confirmed that as the number of samples is increased, the attenuations converge toward port-starboard symmetry, i.e., $\hat{\mathcal{A}}(\theta, \varphi) = \hat{\mathcal{A}}(\theta, -\varphi)$. This follows from the port-starboard symmetry of the engine geometry, mean flow, and equal weight on the positive and negative circumferential modes in the source description. The presence of this symmetry can be useful for future simulation design – half the number of observers can be used. This simplification can also be incorporated into any future prediction models.

However, this port-starboard symmetry of the broadband CDL simulations should not be mistaken for axisymmetry. Results shown at observers not under the flight path indicate that there is a significant effect predicted by CDL due to the three-dimensionality of the duct geometry. This can be seen clearly in Fig. 8, where the attenuation at off-axis angles is shown relative to the corresponding attenuation of the same emission angle under the flight path, i.e., $\hat{\mathcal{A}}(\theta, 0°) - \hat{\mathcal{A}}(\theta, \varphi)$. For the takeoff condition in band 35, upward of 2 dB differences can be seen at certain angles. Data are not available to experimentally verify this effect, but it is plausible given the agreement shown in Fig. 7 under the flight track.
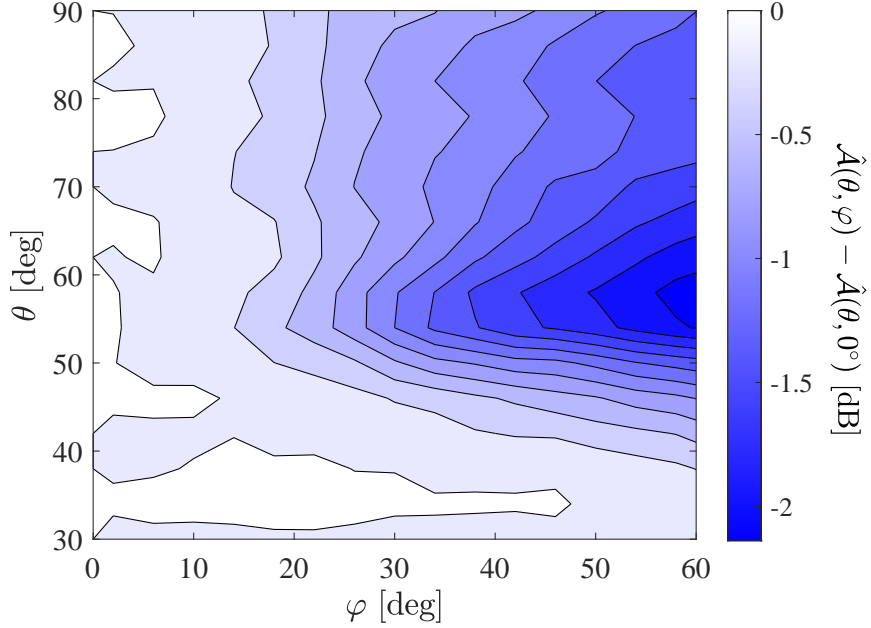
Fig. 8 Far-field integrated attenuation values relative to the corresponding emission angle under the flight track for takeoff, $\mathcal{B} = 35$ as a function of azimuthal angle φ and polar angle θ. $\varphi = 0°$ is along the flight track.

V. Conclusions and Future Work

The primary result of this work is the conclusion that CDL performs similarly to the GRays and Kontos prediction methods in estimating the measured flight test attenuation data, particularly at high power settings. With this validation data alone, and in the current state of the CDL prediction, it does not appear to be worth the additional computational cost to replace the incumbent method of Kontos et al. [5]. However, CDL predictions may prove beneficial in follow-on studies. Only the inlet broadband attenuation has been compared here; tonal inlet attenuation as well as bypass duct attenuation are all potential candidates to be considered. A past validation of CDL for inlet tone prediction of static engine test data showed better agreement at a low power setting than at a higher one. A recently collected flight database [19] on the bypass duct lining of a 787-10 provides an opportunity to examine a different application.

A second, related point is that there are many avenues to refine the computational prediction that may improve the agreement of CDL with flight data. For instance, reducing the grid-related artificial attenuation seen in the hardwall cases could result in more physical, accurate results. A first step toward eliminating one possible source of this attenuation is to incorporate a multigrid solution [15]. Admittedly, this effect is likely the least important for the approach case which has the least agreement with the flight test data. In that case, it is likely that a more realistic source description would result in closer agreement. The challenge is, of course, keeping the source description general enough to be applicable to engines without calibration data.

Third, the ability to estimate the azimuthal variation of liner attenuation is a potential value of CDL that is not available in the Kontos prediction. Without any available experimental data, it is difficult to say how accurate the predicted variations are. Yet the magnitude of the predicted variations with azimuthal angle are large enough that understanding the effect is worth pursuing.

Finally, it is acknowledged that the prediction method of Kontos et al. [5] performed quite well for a wide range of Mach numbers even with the model's independence of flow effects. It is reiterated that using an empirically calibrated method outside of the dataset carries the inherent risks of extrapolation. While the current results are encouraging for the continued limited applicability of this method in conceptual design and system noise assessments, it is still inadvisable to extend use of this tool to liner designs substantially different than the underlying double-degree-of-freedom model data.

12

Acknowledgments

References

[1] National Aeronautics and Space Administration, "NASA Aeronautics: Strategic Implementation Plan 2023," NP-2023-02-3099-HQ, Washington, DC, 2023. URL `https://www.nasa.gov/wp-content/uploads/2021/04/sip-2023-final-508.pdf`.

[2] Wong, J. W., Nesbitt, E., Jones, M. G., and Nark, D. M., "Flight Test Methodology for NASA Advanced Inlet Liner on 737MAX-7 Test Bed (Quiet Technology Demonstrator 3)," *AIAA Paper 2019–2763*, May 2019. doi:10.2514/6.2019-2763.

[3] Brusniak, L., Wong, J., Nesbitt, E., Jones, M. G., and Nark, D. M., "Acoustic Phased Array Quantification of Quiet Technology Demonstrator 3 Advanced Inlet Liner Noise Component," *AIAA Paper 2019-2765*, May 2019. doi:10.2514/6.2019-2765.

[4] Nark, D. M., and Jones, M. G., "Design of an Advanced Inlet Liner for the Quiet Technology Demonstrator 3," *AIAA Paper 2019–2764*, May 2019. doi:10.2514/6.2019-2764.

[5] Kontos, K. B., Kraft, R. E., and Gliebe, P. R., "Improved NASA-ANOPP Noise Prediction Computer Code for Advanced Subsonic Propulsion Systems. Volume 2; Fan Suppression Model Development," NASA/CR-202309, December 1996. URL `https://ntrs.nasa.gov/citations/19970005047`.

[6] Nark, D. M., Farassat, F., Pope, D. S., and Vatsa, V., "The Development of the Ducted Fan Noise Propagation and Radiation Code CDUCT-LaRC," *AIAA Paper 2003-3242*, May 2003. doi:10.2514/6.2003-3242.

[7] Lopes, L. V., and Burley, C. L., "ANOPP2 User's Manual," NASA/TM-2016-219342, October 2016. URL `https://ntrs.nasa.gov/citations/20160014858`.

[8] Dougherty, R. P., "A parabolic approximation for flow effects on sound propagation in nonuniform, softwall, ducts," *AIAA Paper 1999–1822*, May 1999. doi:10.2514/6.1999-1822.

[9] Lan, J. H., "Turbofan Duct Propagation Model," NASA/CR-2001-211245, December 2001. URL `https://ntrs.nasa.gov/citations/20020030747`.

[10] Zlavog, G., and Eversman, W., "Source effects on attenuation in lined ducts. Part I: A statistically based computational approach," *Journal of Sound and Vibration*, Vol. 307, No. 1, 2007, pp. 113–138. doi:10.1016/j.jsv.2007.06.031.

[11] Zlavog, G., and Eversman, W., "Source effects on attenuation in lined ducts. Part II: Statistical properties," *Journal of Sound and Vibration*, Vol. 307, No. 1, 2007, pp. 139–151. doi:10.1016/j.jsv.2007.06.057.

[12] Achunche, I., Astley, J., Sugimoto, R., and Kempton, A., "Prediction of Forward Fan Noise Propagation and Radiation from Intakes," *AIAA Paper 2009–3239*, May 2009. doi:10.2514/6.2009-3239.

[13] Schuster, B., Lieber, L., and Vavalle, A., "Optimization of a Seamless Inlet Liner Using an Empirically Validated Prediction Method," *AIAA Paper 2010–3824*, June 2010. doi:10.2514/6.2010-3824.

[14] Dougherty, R. P., "A Wave-Splitting Technique for Nacelle Acoustic Propagation," *AIAA Paper 1997–1652*, May 1997. doi:10.2514/6.1997-1652.

[15] Nark, D. M., Jones, M. G., Kreitzman, J. R., and Schuster, W., "Bypass Duct Acoustic Liner Design with and without Bifurcation Effects," *AIAA Paper 2024–3269*, June 2024.

[16] Rice, E. J., "Inlet Noise Suppressor Design Method Based upon the Distribution of Acoustic Power with Mode Cutoff Ratio," *Advances in Engineering Science, Vol. 3*, NASA/CP-2001-VOL-3, November 1976, pp. 883–894. URL `https://ntrs.nasa.gov/citations/19770003363`.

[17] Rice, E. J., "Multimodal Far-Field Acoustic Radiation Pattern Using Mode Cutoff Ratio," *AIAA Journal*, Vol. 16, No. 9, 1978, pp. 906–911. doi:10.2514/3.60984.

[18] Eversman, W., "Energy Flow Criteria for Acoustic Propagation in Ducts with Flow," *The Journal of the Acoustical Society of America*, Vol. 49, No. 6A, 1971, pp. 1717–1721. doi:10.1121/1.1912567.

[19] Thomas, R. H., Guo, Y., Clark, I. A., and June, J. C., "Propulsion Airframe Aeroacoustics and Aircraft System Noise Flight Research Test: NASA Overview," *AIAA Paper 2022–2993*, June 2022. doi:10.2514/6.2022-2993.